Entrainment and growth of vortical disturbances in the channel-entrance region - supplementary material

Pierre Ricco[1]† **and Claudia Alvarenga**[1,2]

[1]Department of Mechanical Engineering, The University of Sheffield, S1 3JD Sheffield, United Kingdom

[2]Department of Fluid Dynamics, A*Star Institute of High Performance Computing, Singapore

(Received xx; revised xx; accepted xx)

This supplementary material presents further results that are used in the main paper.

S1. Base flow in regions I and II

According to the method of matched asymptotic expansions, the composite solution reads

$$\overline{\mathbf{U}} = \overline{\mathbf{U}}_{in} + \overline{\mathbf{U}}_{out} - \overline{\mathbf{U}}_{com}, \tag{S1.1}$$

where the subscripts *in*, *out*, and *com* stand for inner, outer, and common, respectively, and $\overline{\mathbf{U}}$ is defined in (2.8). The common part is defined as

$$\overline{\mathbf{U}}_{com} = \lim_{y\to 0} \overline{\mathbf{U}}_{out} = \lim_{\eta\to\infty} \overline{\mathbf{U}}_{in}, \tag{S1.2}$$

where, for the lower channel half,

$$\eta = y\left(\frac{R_\lambda}{2x}\right)^{1/2} = \mathcal{O}(1) \tag{S1.3}$$

is the scaled wall-normal coordinate of the inner solution. As the Reynolds number is large, the inner solution near the inlet corresponds to the Blasius flow (Wilson 1970; Rubin *et al.* 1977; Duck 2005; Buffat *et al.* 2014). It satisfies

$$F''' + FF'' = 0, \tag{S1.4}$$

where the prime indicates differentiation with respect to η. The boundary conditions for equation (S1.4) are $F(0) = 0$, $F'(0) = 0$, and $F' \to 1$ as $\eta \to \infty$. The inner base flow reads

$$\overline{U}_{in} = F', \quad \overline{V}_{in} = \frac{\eta F' - F}{(2xR_\lambda)^{1/2}}. \tag{S1.5}$$

As $R_\lambda \gg 1$, the base-flow viscous effects are negligible in the channel core near the entrance, which is consistent with the use of the boundary-layer approximation of the Navier-Stokes equations. For low and moderate bulk Reynolds numbers, Wang & Longwell (1964), Van Dyke (1969), and Morihara & Cheng (1973) concluded that the vorticity and wall-normal pressure gradients at the entrance are indeed not negligible because they result from the upstream flow influence. However, as the Reynolds number increases, the core flow is not affected by the presence of the walls at leading order. As our work focuses on cases for which the Reynolds numbers are about ten times larger

† Email address for correspondence: p.ricco@sheffield.ac.uk

than in the full Navier-Stokes study by Wang & Longwell (1964), the use of potential flow theory in the channel core and the confinement of the viscous effects near the wall are justified (Rubin *et al.* 1977). In §S2, we compare our results with those obtained via direct numerical simulations (DNS) to confirm the validity of this assumption.

In the inviscid core, the outer flow is described by an inviscid streamfunction ψ,

$$\psi(x,y) = y + R_\lambda^{-1/2}\psi_2(x,y), \tag{S1.6}$$

i.e., $\overline{U}_{out} = \partial\psi/\partial y$ and $\overline{V}_{out} = -\partial\psi/\partial x$. The leading-order term y in (S1.6) defines the uniform streamwise flow. The second-order streamfunction ψ_2 defines the flow due to the channel confinement and to the Blasius boundary layers developing on the channel walls, and satisfies

$$\nabla^2\psi_2 = 0, \tag{S1.7}$$

subject to

$$\psi_2 = 0 \qquad \text{at} \qquad y = 0, 2h, x < 0, \tag{S1.8a}$$

$$\psi_2 = \pm\beta\sqrt{2x} \qquad \text{at} \qquad y = 0 \ (-\text{ sign}),\ 2h \ (+\text{ sign}), x > 0, \tag{S1.8b}$$

where $\beta = \lim_{\eta\to\infty}(\eta - F) = 1.217\ldots$ The boundary conditions (S1.8a) is obtained as follows. The base flow is uniform and streamwise only as $x \to -\infty$ and, as it is not influenced by the presence of the channel walls, no wall-normal base-flow velocity occurs as $x \to -\infty$. Also, no wall-normal base-flow velocity occurs along the horizontal lines $y = 0, 2h$ for $x < 0$ because there is no preferential wall-normal flow direction as the base flow approaches the channel walls. Therefore, $\overline{V}_{out} = 0$ at $y = 0, 2h$ for $x < 0$, i.e., $\partial\psi/\partial x = \partial\psi_2/\partial x = 0$. As we choose $\psi_2 = 0$ as $x \to -\infty$, by integrating $\partial\psi_2/\partial x = 0$ from $x \to -\infty$ for $y = 0, 2h$, it follows that $\psi_2 = 0$ along $y = 0, 2h$ for $x < 0$. The boundary conditions (S1.8b) are obtained by asymptotic matching, i.e., the wall-normal component of the outer velocity must match the outer limit of the base-flow wall-normal velocity of the boundary layer. For the lower-half boundary layer,

$$\overline{V}_{com} = \lim_{y\to 0}\overline{V}_{out} = -\frac{1}{R_\lambda^{1/2}}\frac{\partial\psi_2}{\partial x}\bigg|_{y=0} = \lim_{\eta\to\infty}\overline{V}_{in} = \lim_{\eta\to\infty}\frac{\eta F' - F}{(2xR_\lambda)^{1/2}} = \frac{\beta}{(2xR_\lambda)^{1/2}}. \tag{S1.9}$$

It follows that

$$\psi_2(x) = -\beta\int(2x)^{-1/2}\mathrm{d}x = -\beta\sqrt{2x}, \tag{S1.10}$$

at $y = 0$ for $x > 0$. The condition $\psi_2(x) = \beta\sqrt{2x}$ at $y = 2h$ in (S1.8b) follows from the antisymmetry of the wall-normal velocity. The solution to (S1.7) together with the boundary conditions (S1.8) is found by separation of variables. There exists a full analogy with a heat conduction problem and therefore we refer to page 166 in Carslaw & Jaeger (1959). The solution reads

$$\begin{aligned}\psi_2(x,y) = &\frac{1}{4h}\sin\left(\frac{\pi y}{2h}\right)\int_0^\infty \frac{-\beta\sqrt{2\sigma}\mathrm{d}\sigma}{\cosh[\pi(x-\sigma)/2h] - \cos(\pi y/2h)} + \\ &\frac{1}{4h}\sin\left(\frac{\pi y}{2h}\right)\int_0^\infty \frac{\beta\sqrt{2\sigma}\mathrm{d}\sigma}{\cosh[\pi(x-\sigma)/2h] + \cos(\pi y/2h)}.\end{aligned} \tag{S1.11}$$

The velocity components in the lower channel half read

$$\overline{U}_{out} = \frac{\partial \psi}{\partial y} = 1 + R_\lambda^{-1/2} \frac{\pi}{2h^2} \left\{ \cos\left(\frac{\pi y}{h}\right) \int_0^\infty \frac{-\beta\sqrt{2\sigma}\mathrm{d}\sigma}{\cosh\left[\pi\left(x-\sigma\right)/h\right] - \cos\left(\pi y/h\right)} + \sin^2\left(\frac{\pi y}{h}\right) \int_0^\infty \frac{\beta\sqrt{2\sigma}\mathrm{d}\sigma}{\left\{\cosh\left[\pi\left(x-\sigma\right)/h\right] - \cos\left(\pi y/h\right)\right\}^2} \right\}, \tag{S1.12}$$

$$\overline{V}_{out} = -\frac{\partial \psi}{\partial x} = -R_\lambda^{-1/2} \frac{\pi}{2h^2} \sin\left(\frac{\pi y}{h}\right) \int_0^\infty \frac{\sinh\left[\pi(x-\sigma)/h\right] \beta\sqrt{2\sigma}\mathrm{d}\sigma}{\left\{\cosh\left[\pi\left(x-\sigma\right)/h\right] - \cos\left(\pi y/h\right)\right\}^2}. \tag{S1.13}$$

The integrals in (S1.11), (S1.12) and (S1.13) are computed using the Cavalieri-Simpson rule. The computation of (S1.11) is validated by numerically solving (S1.7) with (S1.8) by use of the Gauss-Seidel method.

The common part of the wall-normal velocity is computed in (S1.9) and the common part of the streamwise velocity in the lower channel half is

$$\overline{U}_{com} = \lim_{y\to 0} \overline{U}_{out} = \lim_{\eta\to\infty} \overline{U}_{in} = 1 + R_\lambda^{-1/2} \frac{\pi}{2h^2} \int_0^\infty \frac{-\beta\sqrt{2\sigma}\mathrm{d}\sigma}{\cosh\left[\pi\left(x-\sigma\right)/h\right] - 1}. \tag{S1.14}$$

The composite solution of the streamwise velocity in the lower channel half is

$$U(x,y) = \overline{U} = F'(\eta(x,y)) + R_\lambda^{-1/2} \frac{\pi}{2h^2} \left\{ \cos\left(\frac{\pi y}{h}\right) \int_0^\infty \frac{-\beta\sqrt{2\sigma}\mathrm{d}\sigma}{\cosh\left[\pi\left(x-\sigma\right)/h\right] - \cos\left(\pi y/h\right)} + \sin^2\left(\frac{\pi y}{h}\right) \int_0^\infty \frac{\beta\sqrt{2\sigma}\mathrm{d}\sigma}{\left\{\cosh\left[\pi\left(x-\sigma\right)/h\right] - \cos\left(\pi y/h\right)\right\}^2} \right\} - R_\lambda^{-1/2} \frac{\pi}{2h^2} \int_0^\infty \frac{-\beta\sqrt{2\sigma}\mathrm{d}\sigma}{\cosh\left[\pi\left(x-\sigma\right)/h\right] - 1}. \tag{S1.15}$$

The streamwise velocity in the upper channel half is symmetric with respect to the centreline. In the composite solution (S1.15), the $\mathcal{O}\left(R_\lambda^{-1/2}\right)$ term in the boundary layer, driven by the $\mathcal{O}\left(R_\lambda^{-1/2}\right)$ term in the last line of (S1.15), is not considered, and therefore the composite solution (S1.15) is of leading-order accuracy and not accurate up to $\mathcal{O}\left(R_\lambda^{-1/2}\right)$.

The composite solution of the wall-normal velocity V, defined in (2.8), in the lower channel half is

$$V(x,y) = k_x^{-1}\overline{V} = \frac{\eta F'(\eta(x,y)) - F(\eta(x,y))}{k_x \left(2xR_\lambda\right)^{1/2}} - R_\lambda^{-1/2} \frac{\pi}{2h^2 k_x} \sin\left(\frac{\pi y}{h}\right) \int_0^\infty \frac{\sinh\left[\pi(x-\sigma)/h\right] \beta\sqrt{2\sigma}\mathrm{d}\sigma}{\left\{\cosh\left[\pi\left(x-\sigma\right)/h\right] - \cos\left(\pi y/h\right)\right\}^2} - \frac{\beta}{k_x \left(2xR_\lambda\right)^{1/2}}. \tag{S1.16}$$

The wall-normal velocity in the upper channel half is antisymmetric with respect to the centreline.

Figure S1 shows the inner and outer solutions, the common part, and the composite solution of the base-flow velocity components for $R_\lambda = 500$ and 2000 at $x = 0.05$. The

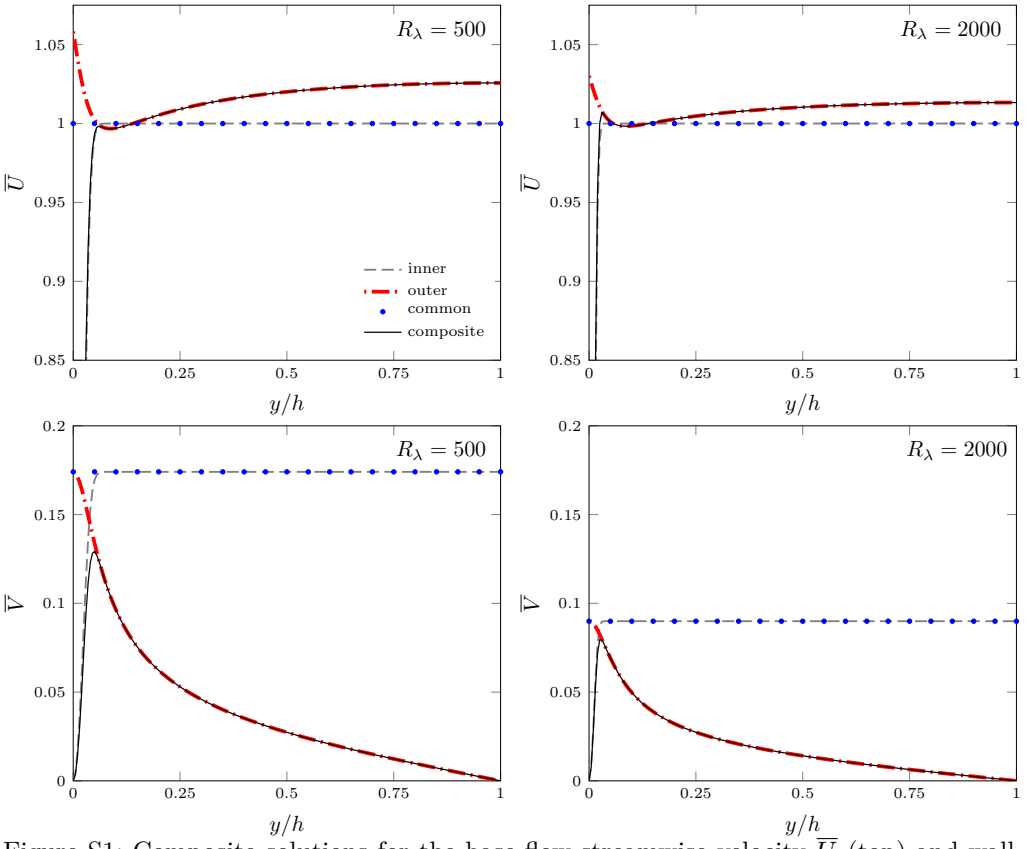

Figure S1: Composite solutions for the base-flow streamwise velocity $\overline{U}$ (top) and wall-normal velocity $\overline{V}$ (bottom) at $x = 0.05$ for two Reynolds numbers.

composite base-flow streamwise velocity, depicted in the top graphs of figure S1, agrees well with the inner Blasius solution across the channel height as the acceleration in the channel core is still small at this x location. The increase of inviscid streamwise velocity balances the decrease within the viscous region to conserve the mass flow rate. The displacement effect of the Blasius boundary layers, given by (S1.9), causes a small streamwise pressure gradient related to the dependence of the displacement streamfunction ψ_2 on the x coordinate, which is negligible at leading order in the near-wall viscous regions. This pressure-gradient effect is weaker than in the case by Xu *et al.* (2020), where the pressure gradient is more intense and non-uniform at leading order from the proximity of the confined region because induced by a converging or divergent channel. In our case, the pressure gradient instead produces a leading-order effect further downstream in region V. The inviscid streamwise velocity is larger than unity near the wall because it accelerates along x to conserve the mass flow rate as the wall-normal velocity decreases from its boundary-layer blowing value as the centreline is approached. This acceleration gives rise to the local near-wall peak in the $\overline{U}$ profile, also reported in Sparrow *et al.* (1964), Panton (2013), and Alizard *et al.* (2018). The peak occurs because the inviscid streamwise velocity is larger than the viscous streamwise velocity deficit of the boundary layer.

The base-flow wall-normal velocity, shown in the bottom graphs of figure S1, agrees well with the viscous solution only in the proximity of the wall, while the two fail to overlap

in the inviscid core, where the composite profile coincides with the outer solution. The composite solution shows a distinct peak located near the wall. As the Reynolds number increases and the viscous effects become more confined near the surface, the peak moves closer to the wall, while it decreases in amplitude and approaches the outer value more closely. The velocity is not exactly zero at the wall. This small slip velocity decreases while the Reynolds number increases as $\mathcal{O}\left(R_\lambda^{-1/2}\right)$ and induces a viscous layer at the next order, which we do not compute.

S2. Base flow in regions V and VI

The inset of figure S2 (top) shows the centreline velocity $\overline{U}_{\rm cen} = \overline{U}(x, y = h)$ computed through the inviscid solution (S1.12) (dash-dotted line) and the boundary-layer equations (2.11)-(2.10) (solid line). The inviscid solution is not zero in a small region upstream of the channel mouth as $\overline{U}_{\rm cen}$ matches the uniform velocity as $x \to -\infty$. The velocity increases as the channel entrance is approached because of the pressure gradient due to the channel confinement. Inside the channel and near the entrance, the centreline velocity $\overline{U}_{\rm cen}$ can be approximated well by the inviscid solution in an overlap region, as evidenced by the inviscid and the viscous solutions showing excellent agreement. However, as the streamfunction formulation in §S1 does not take into account the viscous effects or the base-flow pressure gradient at leading order, the agreement between the inviscid velocity and the viscous velocity computed via the boundary-layer equations (2.11)-(2.10) inevitably deteriorates downstream, where the base-flow pressure gradient is fully influential. The viscous $\overline{U}_{\rm cen}$ then becomes smaller than the inviscid $\overline{U}_{\rm cen}$ because in the former case the core flow is less restricted by the boundary layers over the channel walls as these grow less than in the latter case because they are influenced by the favourable base-flow pressure gradient. The viscous solution is not valid in the very proximity of $x = 0$ because the flow cannot be described by the boundary-layer approximation. Therefore, in order to start the downstream marching procedure, the initial position is selected to be in the range where the inviscid and viscous profiles overlap, the extent of which depends on the Reynolds number. As the Reynolds number increases, this matching region becomes larger as the channel confinement and the pressure gradient become less important.

The base-flow streamwise and wall-normal velocity profiles across the channel are shown in figure S2 for various streamwise positions. The small-x asymptotic profiles (S1.1) are also shown (dashed lines). The flow field approaches the fully-developed regime as it develops downstream: the base-flow streamwise velocity evolves to the parabolic Poiseuille profile, while the wall-normal velocity decreases to zero.

The base-flow streamwise velocity is shown in figure S3 as a function of the streamwise position at various y locations and is compared with data from the literature. There is excellent agreement with the data by Alizard *et al.* (2018) (empty squares) obtained by DNS of the full Navier-Stokes equations, thereby validating our boundary-layer approximation even in the proximity of the channel mouth. The match with the boundary-layer computations by Bodoia & Osterle (1962) (white circles) and the series solution by Sparrow *et al.* (1964) (black circles) is also very good, although near the entrance a slight disagreement is observed with Sparrow *et al.* (1964)'s centreline data and with Bodoia & Osterle (1962)'s data near the wall. The mismatch with the latter could be due to an insufficient numerical resolution due to the high near-wall velocity gradients in the proximity of the channel mouth. The data point by Schlichting (1934) (blue + symbol at $x/(h^2 R_\lambda) = 0.016$), computed by a composite solution of a viscous-flow series and an inviscid-core solution, shows poor agreement because, as pointed out by Bodoia &

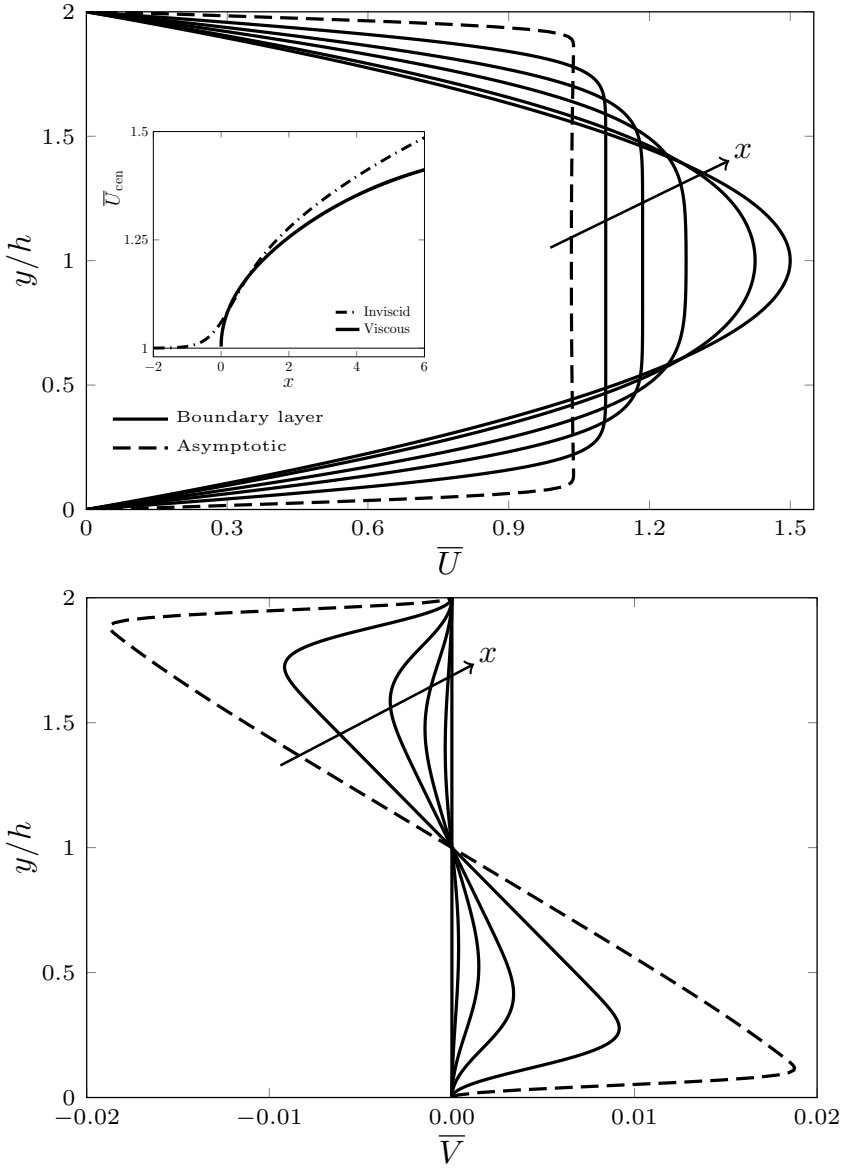

Figure S2: Streamwise (top) and wall-normal (bottom) base-flow velocity profiles. The solid lines denote the solutions at $x/(h^2R_\lambda) = 0.003, 0.012, 0.03, 0.08, 0.4$ obtained by numerically solving the boundary-layer equations (2.11)-(2.10). The dashed lines show the composite solution of the streamwise velocity (S1.15) (top) and of the wall-normal velocity (S1.16) (bottom) at $x/(h^2R_\lambda) = 0.0004$. Inset of top graph: centreline base-flow velocity $\overline{U}_{\rm cen}$ as a function of the streamwise coordinate for $R_\lambda = 75$. The dash-dotted line represents the inviscid solution (S1.15) and the solid line indicates the numerical solution of (2.11)-(2.10).

Osterle (1962), the second derivative of the streamwise velocity, neglected by Schlichting (1934) in the outer solution, has a non-zero value. Collins & Schowalter (1962) improved Schlichting (1934)'s theory by including more terms in the approximation to obtain a

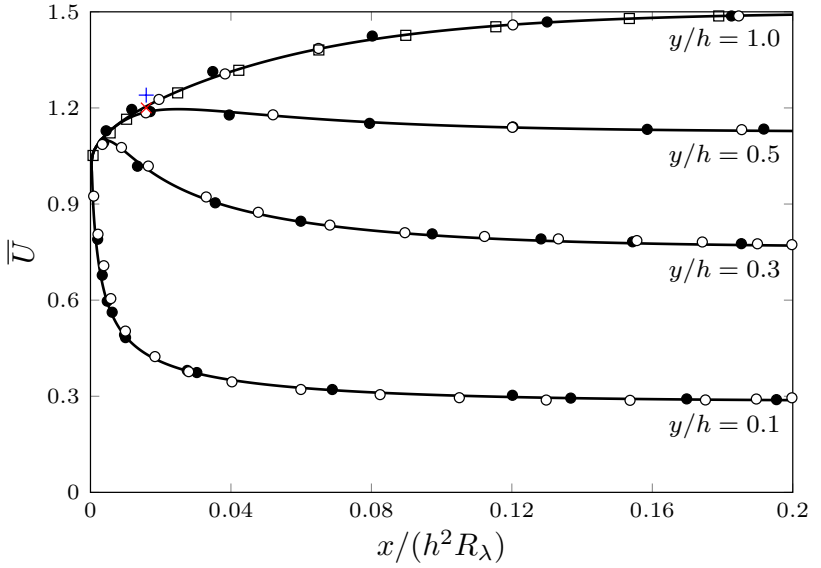

Figure S3: Base-flow streamwise velocity $\overline{U}$ at different y/h locations as a function of the streamwise coordinate, computed by numerically solving the boundary-layer equations (2.11)-(2.10) (solid lines). Symbols: DNS data Alizard *et al.* (2018) (empty squares), boundary-layer data by Bodoia & Osterle (1962) (white circles), series solution by Sparrow *et al.* (1964) (black circles), composite solution by Schlichting (1934) (blue + symbol), and improved composite solution by Collins & Schowalter (1962) (red × symbol).

more accurate result, which matches ours very well (red × symbol at $x/(h^2R_\lambda) = 0.016$).

The downstream adjustment of the pressure gradient can be monitored through the correction pressure function

$$\mathcal{K}\left(\frac{x}{h^2R_\lambda}\right) = \frac{|\Delta\overline{P}^*|}{\rho^* U_\infty^{*2}} - \frac{3\nu^* x^*}{h^{*2}U_\infty^*} = |\Delta\overline{P}| - \frac{3x}{h^2R_\lambda}, \tag{S2.1}$$

which measures the deviation of the base-flow pressure, defined in (2.8), from the fully-developed Poiseuille value. Our computed fully-developed value is $\mathcal{K}_\infty = \lim_{x\to\infty}\mathcal{K}(x) = 0.336$. As shown in figure S4 and consistently with the discussion about the computation of $\overline{U}_{\rm cen}$, the $\mathcal{K}_\infty$ value computed by Schlichting (1934) (blue + symbol) does not match any other, while Collins & Schowalter (1962)'s value (red × symbol) is in excellent agreement with ours and with Bodoia & Osterle (1962)'s (white points), while being only slightly lower than Lundgren *et al.* (1964)'s (orange square). Our data perfectly match Bodoia & Osterle (1962)'s points and are only marginally higher than Sparrow *et al.* (1964)'s (black circles). The comparison with the experimental data by Beavers *et al.* (1970) is also satisfactory (white circles with + symbol), especially when the fully-developed value is approached. This agreement is expected as, arguably, the uncertainty is larger near the channel mouth where the pressure and velocity gradients are largest. Their aspect ratio of 51:1 is almost certainly sufficiently large as their pressure data for the channel with aspect ratio 20:1 leads to values within the experimental uncertainty. The $\mathcal{K}$ values by Asai & Floryan (2004) (white circles with × symbol), obtained from the experimental pressure data in their figure 1 measured in a channel of aspect ratio 27.6:1, are lower than the numerical data. This mismatch could be due to differences in the channel mouth, which

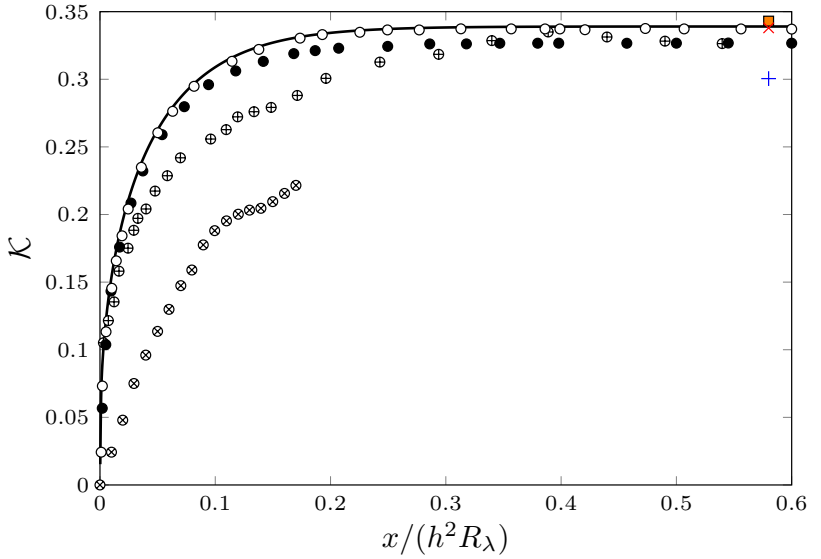

Figure S4: Correction pressure function $\mathcal{K}$, defined in (S2.1), as a function of the streamwise coordinate, computed by numerically solving the boundary-layer equations (2.11)-(2.10) (solid line). Symbols: series solution by Lundgren *et al.* (1964) (orange square), experimental data by Beavers *et al.* (1970) (white circles with + symbol) and by Asai & Floryan (2004) (white circles with × symbol). The legend for the black and white circles, the blue + symbol, and the red × symbol is the same as in figure S3.

are not described in Asai & Floryan (2004) because their focus was further downstream, near the fully-developed region. Their asymptotic value, $\mathcal{K}_\infty = 0.23$, computed by fitting their large-x formula $\mathcal{K} = \mathcal{K}_\infty + C\exp(-\xi x)$ to the experimental data (where C is a constant and ξ is an eigenvalue), is much lower than our numerical value.

We now define boundary-layer thicknesses to quantify the diffusion of the viscous effects as the flow develops downstream. They are defined as

$$\delta_k = \Delta_k \int_0^h \left[1 - \frac{\overline{U}(x,y)}{\overline{U}_{\rm cen}(x)}\right] \mathrm{d}y, \tag{S2.2}$$

where $k = h$ identifies the boundary thickness that matches the half channel height in the fully-developed downstream limit ($\Delta_h = 3$ is obtained by substituting $\delta_h = h$, $\lim_{x\to\infty}\overline{U}(x,y) = 3y(2-y/h)/2h$, and $\lim_{x\to\infty}\overline{U}_{\rm cen} = 3/2$ into (S2.2)) and $k =$ LWG,CH denotes the boundary thickness that matches the one employed by LWG99 as $x \to 0$, i.e., $\delta_{\rm LWG} = (2x/R_\lambda)^{1/2}$ ($\Delta_{\rm LWG,CH} = \beta^{-1} = 0.822$ is obtained by substituting (S1.15) into (S2.2)). Figure S5 (left) shows the boundary-layer thicknesses as functions of the streamwise coordinate. The thickness $\delta_{\rm LWG,CH}$ in our channel-flow case is thinner than the corresponding Blasius-flow $\delta_{\rm LWG}$ because of the accelerating core caused by the favourable pressure gradient.

We also quantify the entry length, i.e., the distance from the channel mouth where region V ends and the fully-developed region VI starts. The entry length is typically defined by the streamwise location where $\overline{U}_{\rm cen}$ reaches 99% of its fully-developed value. We can first use equation (23) in Durst *et al.* (2005), i.e., $x_{e,u} = 2h\left[0.4787 + (2C_{e,u}hR_\lambda)^{1.6}\right]^{1/1.6}$, where $C_{e,u} = 0.0442$. As we operate under the assumption $R_\lambda \gg 1$, Durst *et al.* (2005)'s equation reduces to $x_{e,u} = 4C_{e,u}h^2R_\lambda$, which is consistent with the scaling adopted in figure S3. We compute $C_{e,u} = 0.043$, which is within the uncertainty range provided by

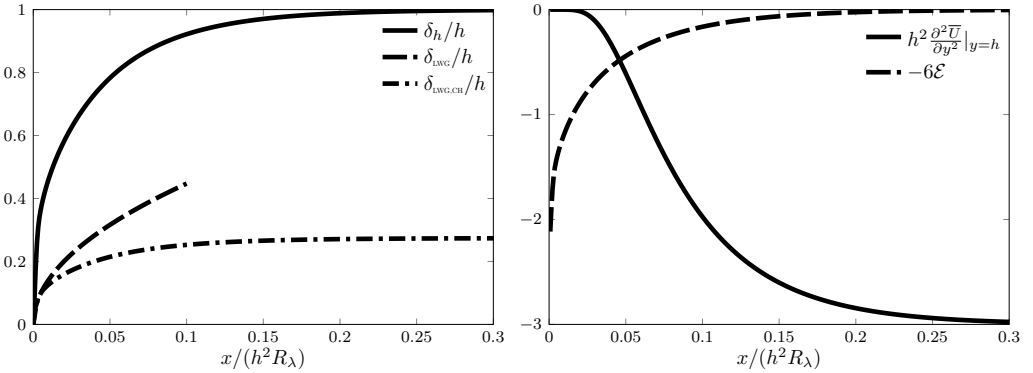

Figure S5: Left: Boundary-layer thicknesses δ_h, δ_{LWG}, and $\delta_{\text{LWG,CH}}$ as functions of the streamwise coordinate. Right: Second derivative of the streamwise velocity at the centreline and average error $\mathscr{E}$, defined in the text and measuring the deviation of the $\overline{U}$ profile from the Poiseuille solution, as functions of the streamwise coordinate.

Durst *et al.* (2005). We also quantify the entrance region as $x_{e,pres} = 4C_{e,pres}h^2R_\lambda$, i.e., the streamwise distance from the channel mouth where $\mathcal{K} = 0.99\mathcal{K}_\infty$, that is, where the pressure gradient has reached its fully developed constant value. We compute $C_{e,pres} = 0.054$.

Crabtree, Küchemann, and Sowerby on page 440 of Rosenhead (1963) remark that in a pipe entrance flow:"...the whole of the fluid across a section becomes influenced by viscosity before the parabolic distribution is reached." We can examine this statement in our case of channel flow, although they do not specify how the diffusion of viscous effects is defined mathematically. The flow development to the Poiseuille parabolic profile is already quantified by the entry length $x_{e,u}$, based on the downstream evolution of $\overline{U}_{\text{cen}}$, but we also further monitor it by an adjustment length $x_{e,pois} = 4C_{e,pois}h^2R_\lambda$, defined as the streamwise location where the average difference between the streamwise velocity and the Poiseuille velocity, i.e., $\mathscr{E}(x) = (1/h)\int_0^h |\overline{U}(x,y) - 3y(2-y/h)/2h|\mathrm{d}y$ (shown by the dashed line in figure S5, right), has decayed to 1% of $\lim_{x\to 0}\mathscr{E} = 1$. We find $C_{e,pois} = 0.038$, i.e., comparable with $C_{e,u}$. The diffusion of viscous effects can be quantified by two adjustment lengths. We first obtain $x_{e,u2} = 4C_{e,u2}h^2R_\lambda$, i.e., the downstream distance from the channel mouth where the second derivative of the streamwise velocity with respect to the wall-normal direction at the centreline, $\partial^2\overline{U}/\partial y^2|_{y=h}$ (shown by the solid line in figure S5, right), is 99% of its fully-developed value. We choose this quantity because it represents wall-normal viscous effects and the centreline is the last wall-normal location where the viscous diffusion from the wall is felt. We compute $C_{e,u2} = 0.072$. We then find $x_{e,\delta} = 4C_{e,\delta}h^2R_\lambda = 0.052$, i.e., the downstream distance from the entrance where δ_h=0.99h. Table S1 summarizes the computed entrance lengths.

We therefore find that $C_{e,u2}$, $C_{e,\delta} > C_{e,u}, C_{e,pois}$, i.e., the flow becomes viscous for the whole wall-normal extent of the channel slightly downstream from where the flow can be considered in good agreement with the Poiseuille profile. Therefore, there does not exist a distinct streamwise region along which viscous diffusion affects the whole wall-normal extent of the channel and the velocity profile has not yet developed to the parabolic profile. It remains to be verified whether this streamwise region exists in a pipe flow, as stated by Crabtree, Küchemann, and Sowerby. The adjustment length $x_{e,u2}$, based on the second wall-normal derivative of the streamwise velocity at the centreline, is the most conservative amongst the four lengths, as also visually evident in figure S5 (right).

Criterion	$\mathrm{d}\overline{P}/\mathrm{d}\overline{x}$	$\mathscr{E}$	$\overline{U}_p(y=h)$	δ_h	$\left.\frac{\partial^2\overline{U}}{\partial y^2}\right\vert_{y=h}$
Parameter	$C_{e,pres}$	$C_{e,pois}$	$C_{e,u}$	$C_{e,\delta}$	$C_{e,u2}$
	0.054	0.038	0.043	0.052	0.072
Entry length	$x_{e,pres}/(h^2R_\lambda)$	$x_{e,pois}/(h^2R_\lambda)$	$x_{e,u}/(h^2R_\lambda)$	$x_{e,\delta}/(h^2R_\lambda)$	$x_{e,u2}/(h^2R_\lambda)$
	0.216	0.152	0.172	0.208	0.288

Table S1: Entrance lengths according to definitions presented in the text.

REFERENCES

Alizard, F., Cadiou, A., Le Penven, L., Di Pierro, B. & Buffat, M. 2018 Space-time dynamics of optimal wavepackets for streaks in a channel entrance flow. *J. Fluid Mech.* **844**, 669–706.

Asai, M. & Floryan, J.M. 2004 Certain aspects of channel entrance flow. *Phys. Fluids* **16** (4), 1160–1163.

Beavers, G.S., Sparrow, E.M. & Magnuson, R.A. 1970 Experiments on hydrodynamically developing flow in rectangular ducts of arbitrary aspect ratio. *Int. J. Heat Transfer* **13**, 689–702.

Bodoia, J.R. & Osterle, J.F. 1962 Finite difference analysis of plane Poiseuille and Couette flow developments. *App. Sc. Res.* **10** (1), 265–276.

Buffat, M., Le Penven, L., Cadiou, A. & Montagnier, J. 2014 DNS of bypass transition in entrance channel flow induced by boundary layer interaction. *Eur. J. Mech. - B/Fluids* **43**, 1–13.

Carslaw, H.S. & Jaeger, J.C. 1959 *Conduction of heat in solids*. Clarendon Press.

Collins, M. & Schowalter, W.R. 1962 Laminar flow in the inlet region of a straight channel. *Phys. Fluids* **5**, 1122–1124.

Duck, P.W. 2005 Transient growth in developing plane and Hagen Poiseuille flow. *Proc. Royal Soc. London. Series A.* **461**, 1311–1333.

Durst, F., Ray, S., Ünsal, B. & Bayoumi, O.A. 2005 The development lengths of laminar pipe and channel flows. *J. Fluids Eng.* **127** (6), 1154–1160.

Lundgren, T.S., Sparrow, E.M. & Starr, J.B. 1964 Pressure drop due to the entrance region in ducts of arbitrary cross section. *Trans. ASME J. Basic Eng.* pp. 620–626.

Morihara, H. & Cheng, R.T.S. 1973 Numerical solution of the viscous flow in the entrance region of parallel plates. *J. Comp. Phys.* **11** (4), 550–572.

Panton, R. 2013 *Incompressible Flow*. Wiley-Interscience – Fourth Edition.

Rosenhead, L. 1963 *Laminar Boundary Layers*. Dover.

Rubin, S.G., Khosla, P.K. & Saari, S. 1977 Laminar flow in rectangular channels. *Computers and Fluids* **5**, 151–173.

Schlichting, H. 1934 Laminar channel entrance flow. *Z. Angew. Math. Mech.* **14**, 368–373.

Sparrow, E.M., Lin, S.H. & Lundgren, T.S. 1964 Flow development in the hydrodynamic entrance region of tubes and ducts. *Phys. Fluids* **7** (3), 338–347.

Van Dyke, M. 1969 Entry flow in a channel. *J. Fluid Mech.* **44**, 813–823.

Wang, Y.L. & Longwell, P.A. 1964 Laminar flow in the inlet section of parallel plates. *AIChE J.* **10** (3), 323–329.

Wilson, S.D.R. 1970 Entry flow in a channel. Part 2. *J. Fluid Mech.* **46**, 787–799.

Xu, D., Liu, J. & Wu, X. 2020 Görtler vortices and streaks in boundary layer subject to pressure gradient: excitation by free stream vortical disturbances, nonlinear evolution and secondary instability. *J. Fluid Mech.* **900** (A15).